JGR Solid Earth

Supporting Information for

Changes in seismic attenuation due to fracturing and fluid migration during the 2016-2017 Central Italy seismic sequence

[1,2*]Simona Gabrielli, [1]Aybige Akinci, [1]Guido Ventura, [3]Ferdinando Napolitano, [4,5]Edoardo Del Pezzo and [2,6] Luca De Siena

1) Istituto Nazionale di Geofisica e Vulcanologia, Via di Vigna Murata 605, 00143 Roma, Italy
2) University of Aberdeen, School of Geosciences, Meston Building, Aberdeen, AB24 3UE, Scotland, UK
3) Università degli Studi di Salerno, Dipartimento di Fisica "E.R. Caianiello", Via Giovanni Paolo II 132, 84084, Fisciano, SA, Italy
4) Istituto Nazionale di Geofisica e Vulcanologia, Osservatorio Vesuviano, Via Diocleziano, 328, 80125, Napoli, Italy
5) Istituto Andaluz de Geofisica, Universidad de Granada, Calle del Prof. Clavera, 12, 18071 Granada, Spain
6) Institute of Geosciences, Johannes Gutenberg University, J.-J.-Becher-Weg 21 D-55128, University of Mainz, Germany

Contents of this file

Introduction

The following Supporting Information are:

- a more detailed description of the methods and functions used for the coda wave attenuation tomography;
- Figures S1-S4 are related to both the peak delay analysis and the coda wave onset;
- Figures S5-S9 are related to the tomographic imaging of the coda-wave attenuation (kernels, checkerboard tests);
- Figures S10-S15 are the results for peak delay, coda-wave attenuation at the frequencies of 3, 6 and 12 Hz. Figure S16 is an example of the parameter separation plot.

Text S1: Onset of diffusion, sensitivity kernels and resolution tests.

A necessary condition to fulfill the assumption of $Q_c^{-1} = Q_i^{-1}$ is to measure this quantity over diffusive coda wave packets (Calvet and Margerin, 2013). Q_c^{-1} shows a small decreasing trend (with moving mean values spanning between 0.009 and 0.003) using the chosen coda window; however, the slope has low values (e.g., -0.0001 at 1.5 Hz), of the order of those chosen to map absorption across the Alpine range (Figure S4 – compare with Figure 5c in Mayor et al., 2016).

The choice of $2t_S$ as starting lapse time (t) implicates different sampling for different hypocentral distances ($r_{i,j}$). This is considered by implementing multiple scattering sensitivity kernels depending on lapse time, hypocentral distances, frequency, and the average scattering characteristics of the crust. These characteristics are defined using estimates of seismic albedo (B_0 and extinction length *Le*, Del Pezzo et al. (2018).

Adopting the Paaschens (1997) approximation of the Energy Transport Equation solution in three dimensions, the seismogram energy envelope is defined as:

$$E_{i,j}^{3D}\left[r_{i,j}, t, B_0, Le^{-1}, v\right] \approx \frac{W_0 exp[-Le^{-1}vt]}{4\pi r_{ij}^2 v}\,\delta\left[t - \frac{r_{ij}}{v}\right] + W_0 H\left[t - \frac{r_{ij}}{v}\right] \cdot$$

$$\frac{\left(1-\frac{r_{ij}^2}{v^2t^2}\right)^{\frac{1}{8}}}{\left(\frac{4\pi vt}{3B_0Le^{-1}}\right)^{\frac{3}{2}}} \cdot expexp[-Le^{-1}vt]F\left[vtB_0Le^{-1}\left(1-\frac{r_{ij}^2}{v^2t^2}\right)^{3/4}\right] \qquad (5)$$

where δ is the Dirac delta, H the Heaviside step functions, W_0 the source energy, and v the seismic velocity (here 3.5 km/s). F is expressed as:

$$F[x] = e^x\sqrt{1 + 2.026/x} \qquad (6)$$

This function has been calculated using the estimates of the Extinction Length $Le^{-1} = \eta_i + \eta_s$ and the Seismic albedo $B_0 = \eta_s Le^{-1}$ for each frequency band obtained from the Multi Lapse Time Window Analysis performed by Akinci et al. (2020) with the same dataset. Using the hypothesis of Pacheco and Snieder (2005), we define the spatial sensitivity ($K_{i,j}^{3D}$) of the energy envelope at a given lapse time (at half of the selected coda window) as:

$$K_{i,j}^{3D}[\varrho, t, B_0, Le^{-1}, v] = \int_0^T E^{3D}\left[r_{s\varrho}, \tau, B_0, Le^{-1}, v\right] \times E^{3D}\left[r_{\varrho r}, t, B_0, Le^{-1}, v\right] d\tau (7)$$

where ρ is the space point with coordinates *i,j,z,* $r_{s\varrho}$ is the point-to-source distance, $r_{\varrho r}$ is the point-to-receiver distance, and τ the integration variable.

Del Pezzo et al. (2018) implemented the solution by convolution of the first (coherent) and second (multiple scattering) terms in Eq. (5) through a dense grid coverage the medium. The kernels suffer poles at the source and station locations. We linearly interpolate the kernels in space using the nearest eight nodes to provide the kernel values at these points. In **Figure S5a** we present the 2D flattening of a 3D sensitivity kernel (**Figure S5b)** performed by averaging sensitivity over depth (Gabrielli et al., 2020; Sketsiou et al., 2020). The highest sensitivity values (in yellow) are recorded at source and receiver locations, while the area between them is poorly covered for single-station measurements. Despite this lack of sensitivity, the high density of sources and stations (**Figure S2-S3**) allows to recover the central areas.

The kernel functions are used to build the rows of the inversion matrix of a grid of constant step of 7.5 km, after normalization for the source-receiver pair's total weight. The mapping is performed with the inversion scheme described by De Siena et al. (2017), with the hypothesis that the energy is entirely lost inside the predefined grid. The linear inverse problem (**d** = **Gm**) solves for the spatial distribution of Q_c^{-1} at each node. **d** is the data vector for each of the N source-station measurements of Q_c^{-1}, **m** is a model parameter vector M x 1, where M is the number of nodes, and **G** is a N x M matrix defined by the kernel for each source-receiver pair (Sketsiou et al., 2020):

$$\begin{bmatrix} Qc_1 \\ Qc_2 \\ \vdots \\ Qc_N \end{bmatrix} = \begin{bmatrix} k_{11} & k_{12} & \cdots & k_{1M} \\ k_{21} & k_{22} & \cdots & k_{2M} \\ \vdots & \vdots & \ddots & \cdots \\ k_{N1} & k_{N2} & \cdots & k_{NM} \end{bmatrix} \begin{bmatrix} Q_c^1 \\ Q_c^2 \\ \vdots \\ Q_c^M \end{bmatrix}$$

where k_{ij} is the source-receiver pair, with $i = 1, \ldots, N$ and $j = 1, \ldots, M$. Q_{cN} represents the Q_c for each source-receiver pair, while Q_c^M corresponds to the Q_c associated at each block of the map. A zero-

order Tikhonov regularization is used to solve the inverse problem. The damping parameter is chosen from the L-curve, plotted as the log-log of the norm of the regularized solution versus the residual norm. We have tested various damping parameters between the regularized solution's size and ther fit to data. Finally, we selected for each frequency band a value between 0.3 and 0.6 as the best damping parameters based on the L-curve shape. **Figure S6** is an example L-curve obtained at 6 Hz for the 2016-2017 dataset, where we selected 0.4 (in red) as the damping parameter. The choice of a damping parameter is fundamental to avoid an over-damped (high damping parameter) or rough (low damping parameter) solution.

We tested our resolution by performing checkerboard tests with multiple grid node spacing (Supplementary Material, **Figs. S7-9**). The checkerboard test obtained from applying the kernel functions described above clearly allows the interpretation of the central area, both for the pre and sequence datasets.

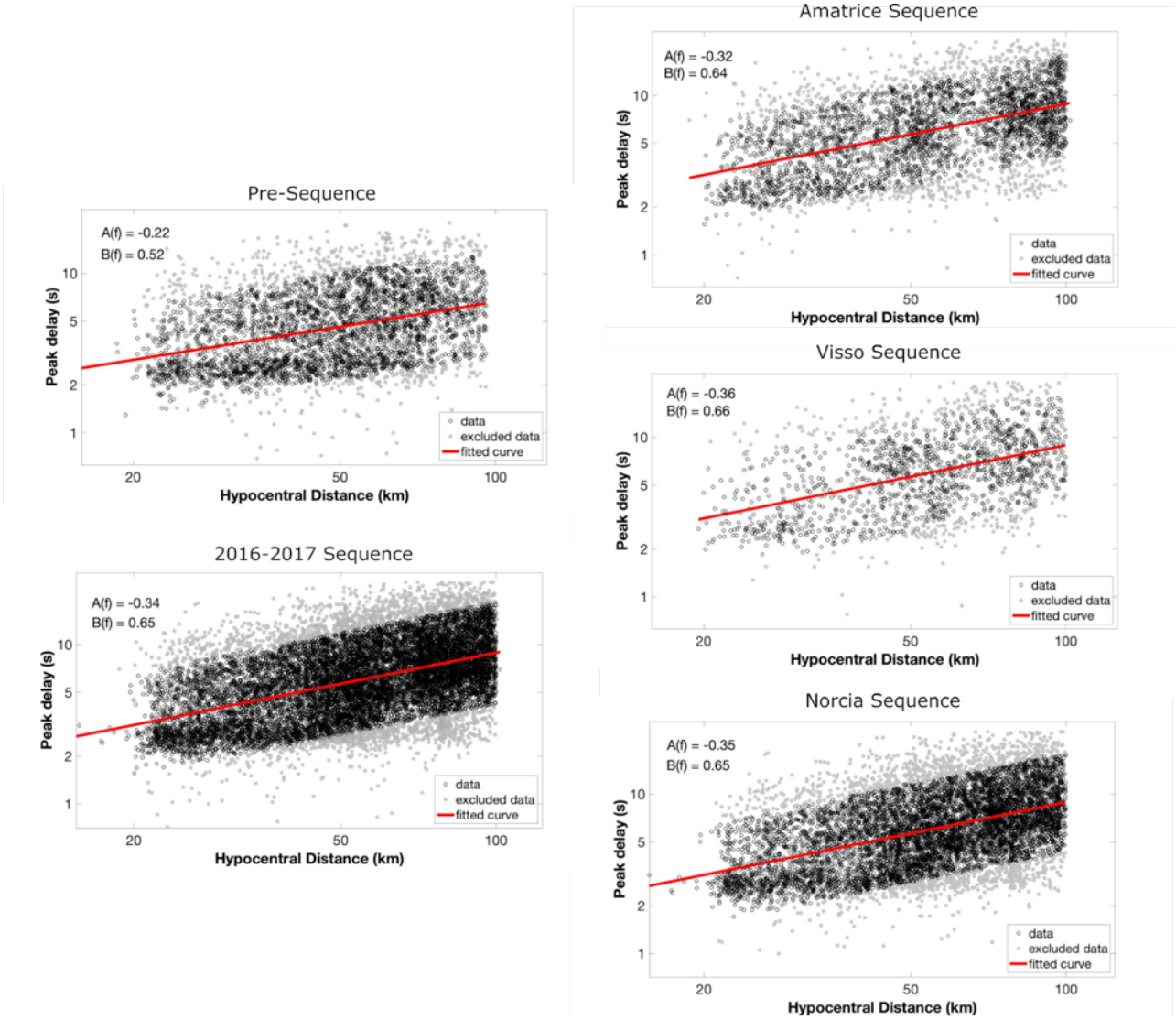

Figure S1 Log-log plot of peak delay (s) as a function of the of the hypocentral distances (km) for the pre-sequence, 2016-2017 sequence and single sequences at 1.5 Hz. The dashed red line represents the best linear fit for the peak delay measurement (black circles). Gray circles are the outliers, excluded because: 1) the norm of the residuals between the data and fit exceeds 1.5 times the standard deviation and/or; 2) the lag time does not range between 0.1 s and 24 s, and the peak delay could be influenced by transient phases interacting with the mantle. A(f) and B(f) are the coefficients of the best linear fit.

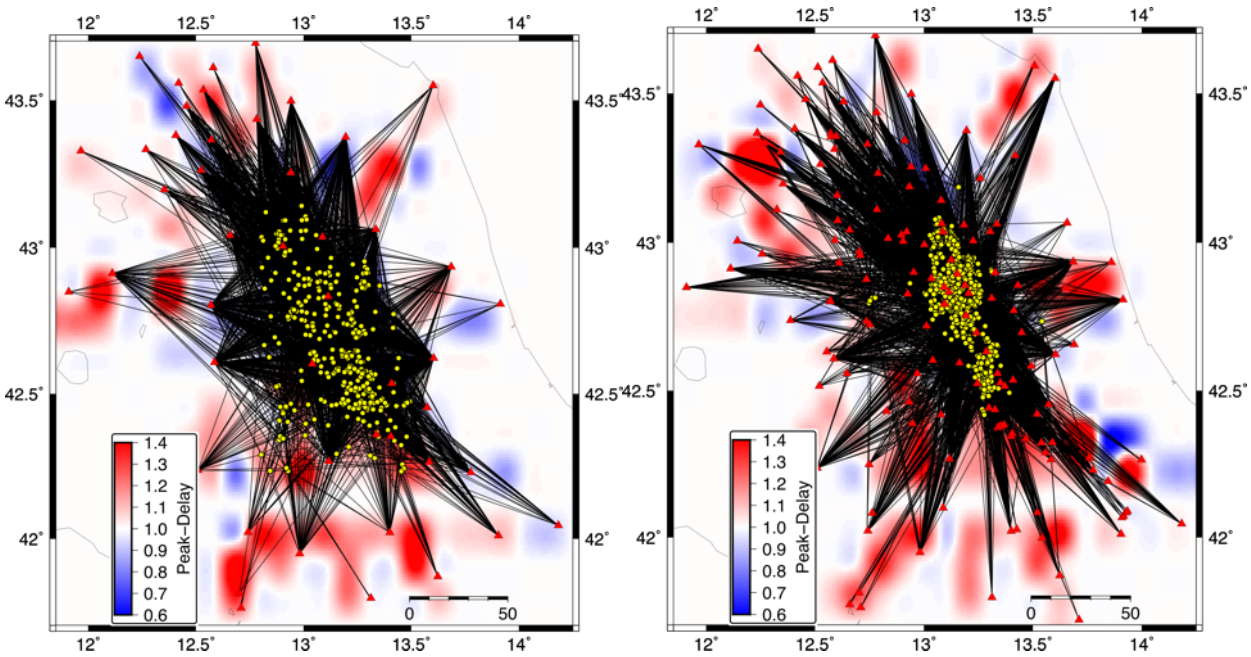

Figure S2 Ray distribution for the pre-sequence (left) and sequence (right) dataset, plotted on the peak delay map of the 2016-2017 sequence at 6 Hz. Yellow dots represent the events and the red triangles the seismic stations.

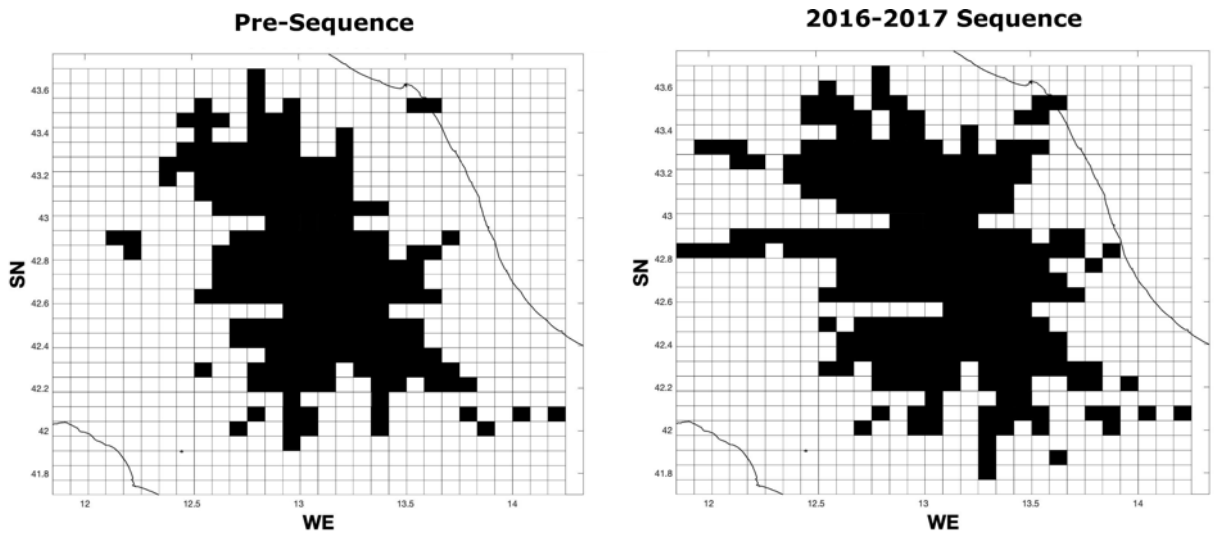

Figure S3 Hit Count map, showing the number of rays passing through each cell for the pre-sequence (left) and the 2016-2017 sequence (right) datasets. The blocks crossed by 10 or more ray paths are colored in black.

a)

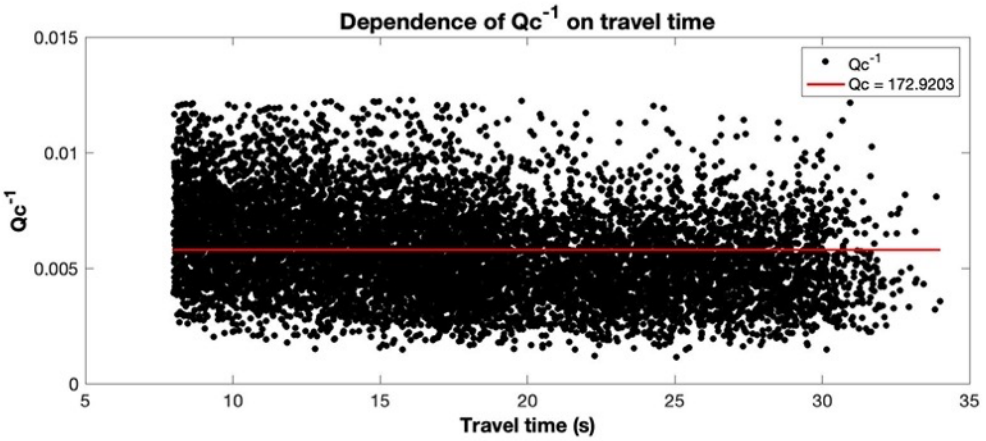

b)

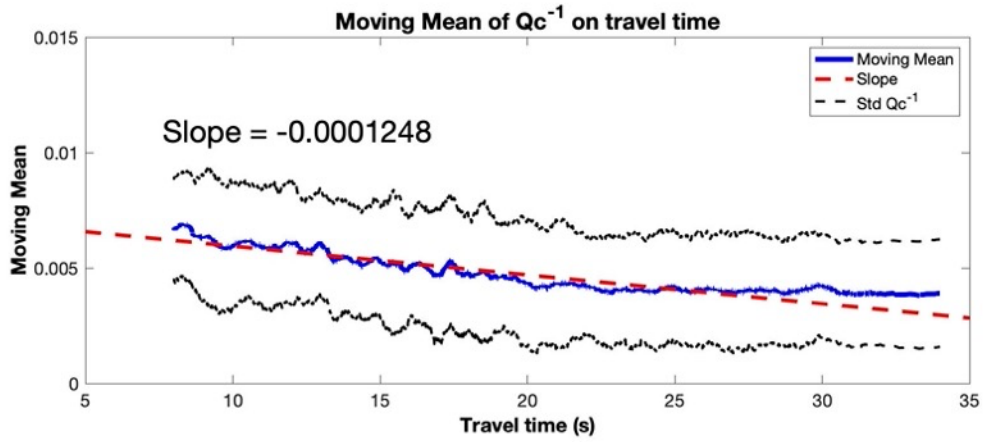

Figure S4 a) Dependence of Q_c^{-1} *on travel time (s) for the 2016-2017 dataset at* f_c *= 1.5 Hz and b) its moving mean. a) Black dots are the* Q_c^{-1} *for each waveform obtained from the linear approach approximation in Eq. (4). The red line represents the average* Q_c^{-1}*. b) The blue line is the moving mean of the* Q_c^{-1}*in (a), the black lines its standard deviation and the red dashed line its slope.*

a)

b)

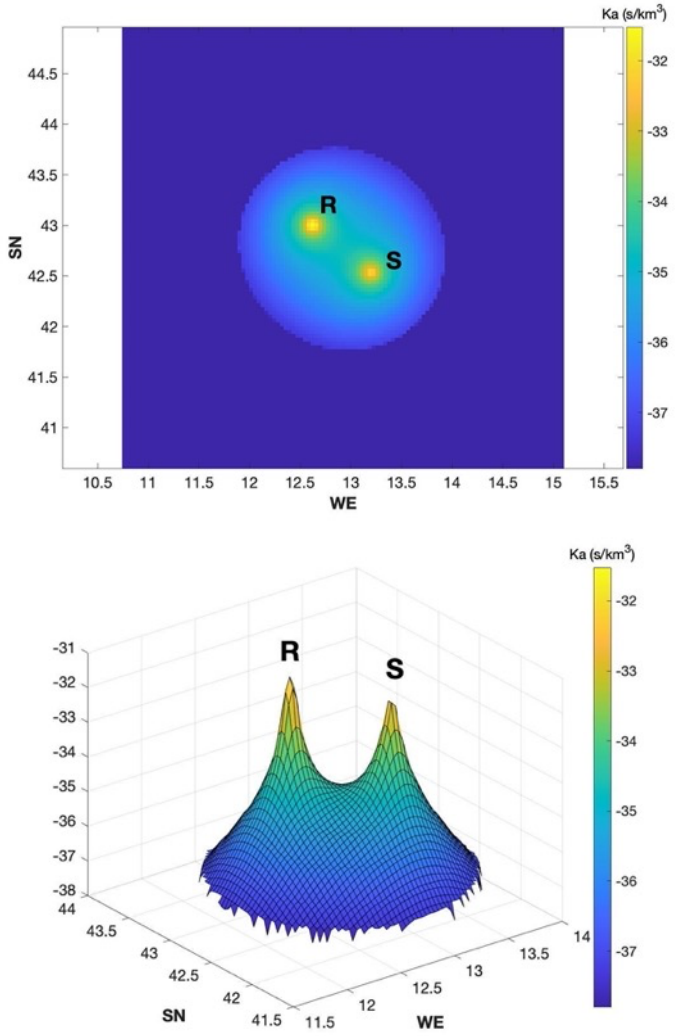

Figure S5 Map view of the sensitivity kernel at a depth of 4 km for a source (S) - receiver (R) pair at a fc = 6 Hz in 2D (a) and 3D (b).

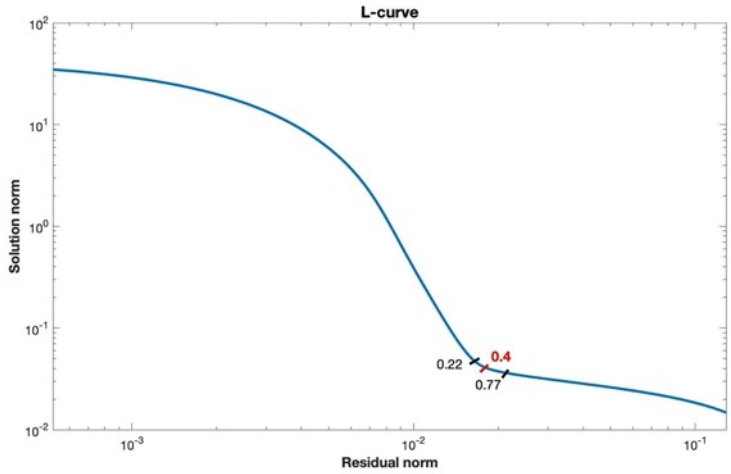

Figure S6 L-curve for the 2016-2017 dataset at f_c = 6 Hz. In red, the chosen damping parameter (0.4) for the linear inversion at this frequency and for this dataset.

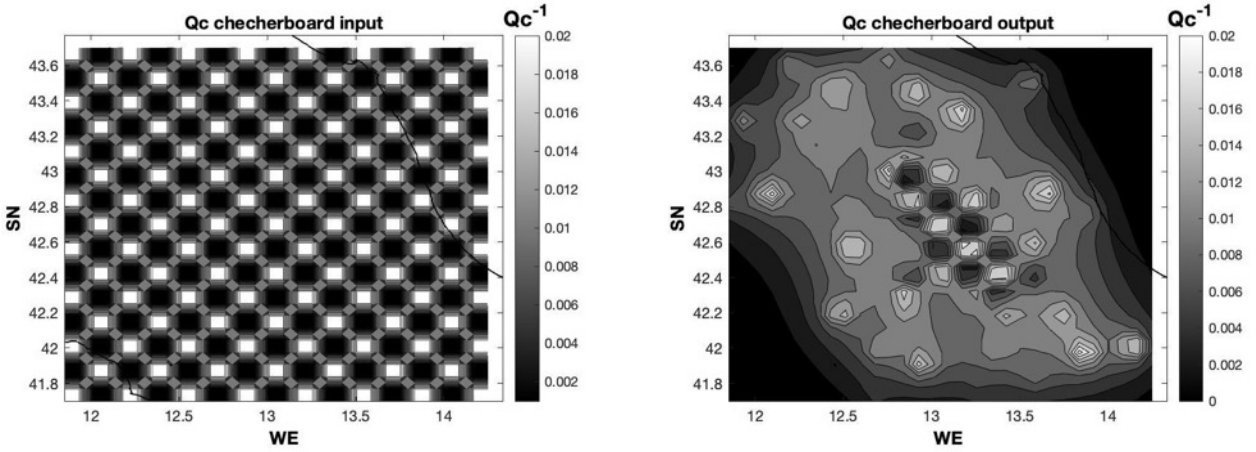

Figure S7 Checkerboard test at 3 Hz for the pre-sequence dataset

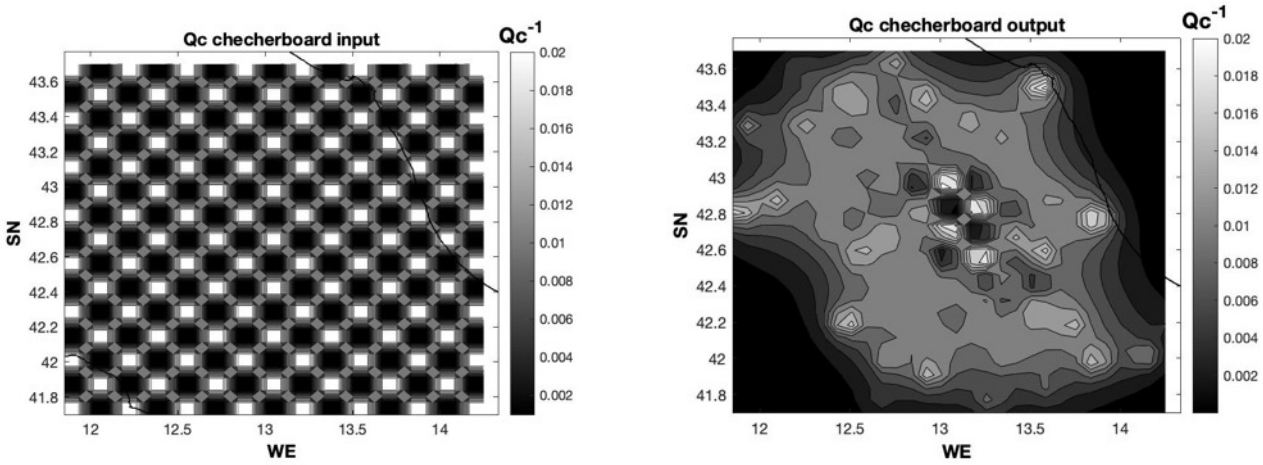

Figure S8 Checkerboard test at 3 Hz for the entire 2016-2017 sequence

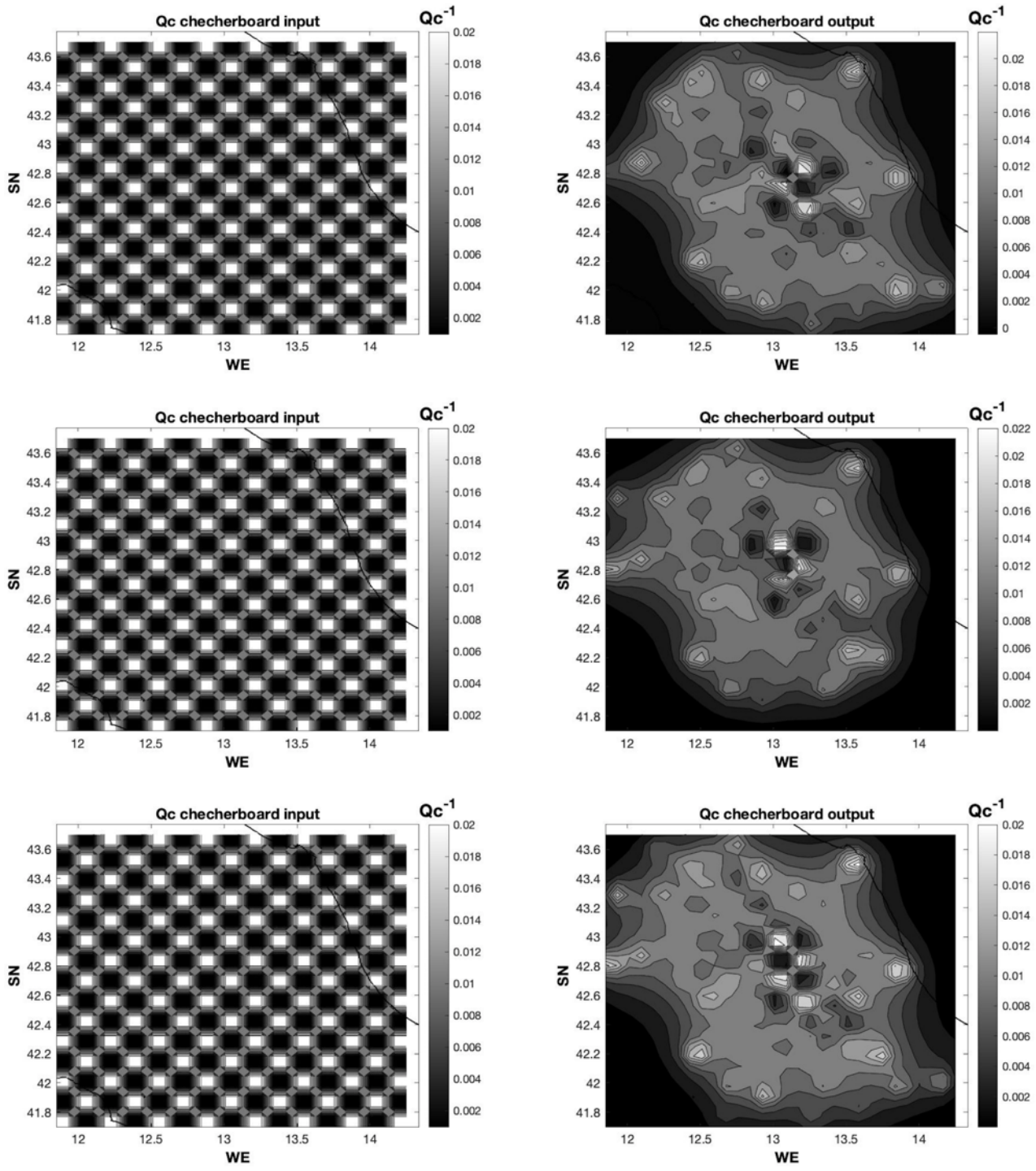

Fig. S9 Checkerboard tests at 3 Hz of each sequence (starting from above: Amatrice, Visso and Norcia)

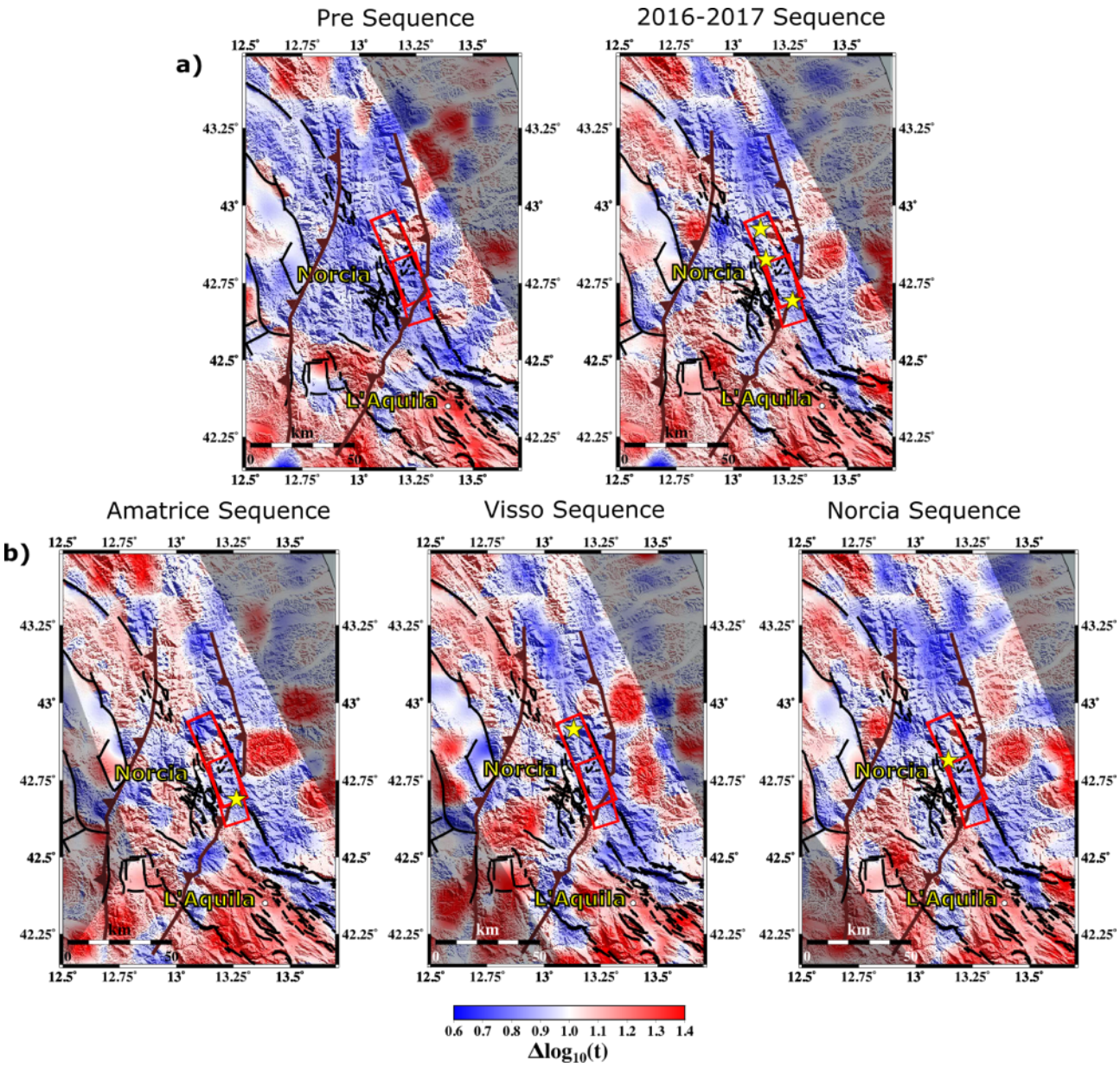

Figure S10 Spatial and temporal variation of Peak Delay at f_c = 3 Hz over the a) Pre-sequence, the 2016-2017 sequence and b) three individual sequences time frames. Red boxes are the fault plane for the Amatrice and the Norcia earthquakes and black lines the faults from ITHACA catalogue. Brown lines are the main thrust of the area. The stars indicate the main shocks of each 2016-2017 sequence. The maps have been restricted to the area of interest.

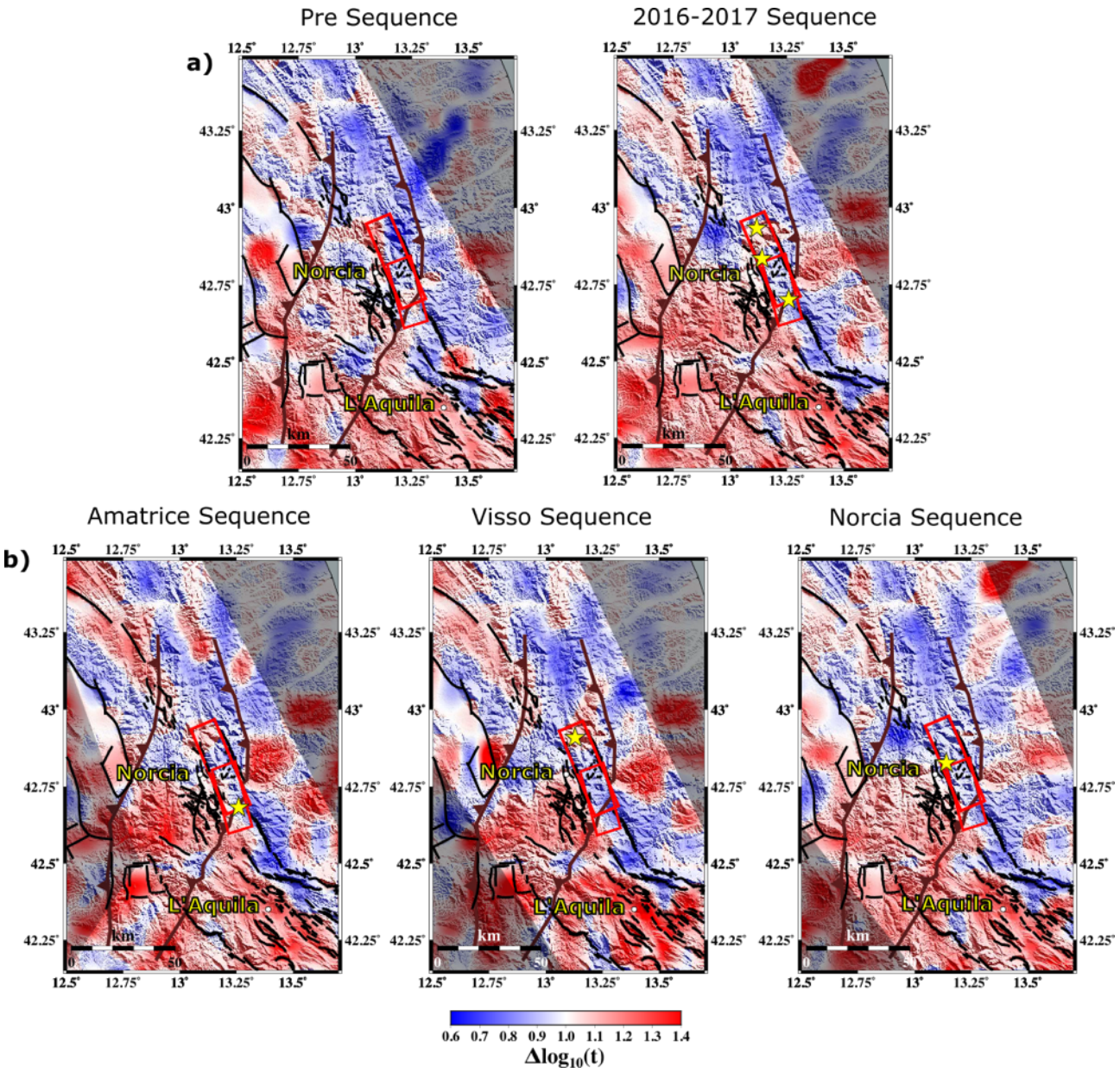

Figure S11 Spatial and temporal variation of Peak Delay at f_c = 6 Hz over the a) Pre-sequence, the 2016-2017 sequence and b) three individual sequences time frames. Red boxes are the fault plane for the Amatrice and the Norcia earthquakes and black lines the faults from ITHACA catalogue. Brown lines are the main thrust of the area. The stars indicate the main shocks of each 2016-2017 sequence. The maps have been restricted to the area of interest.

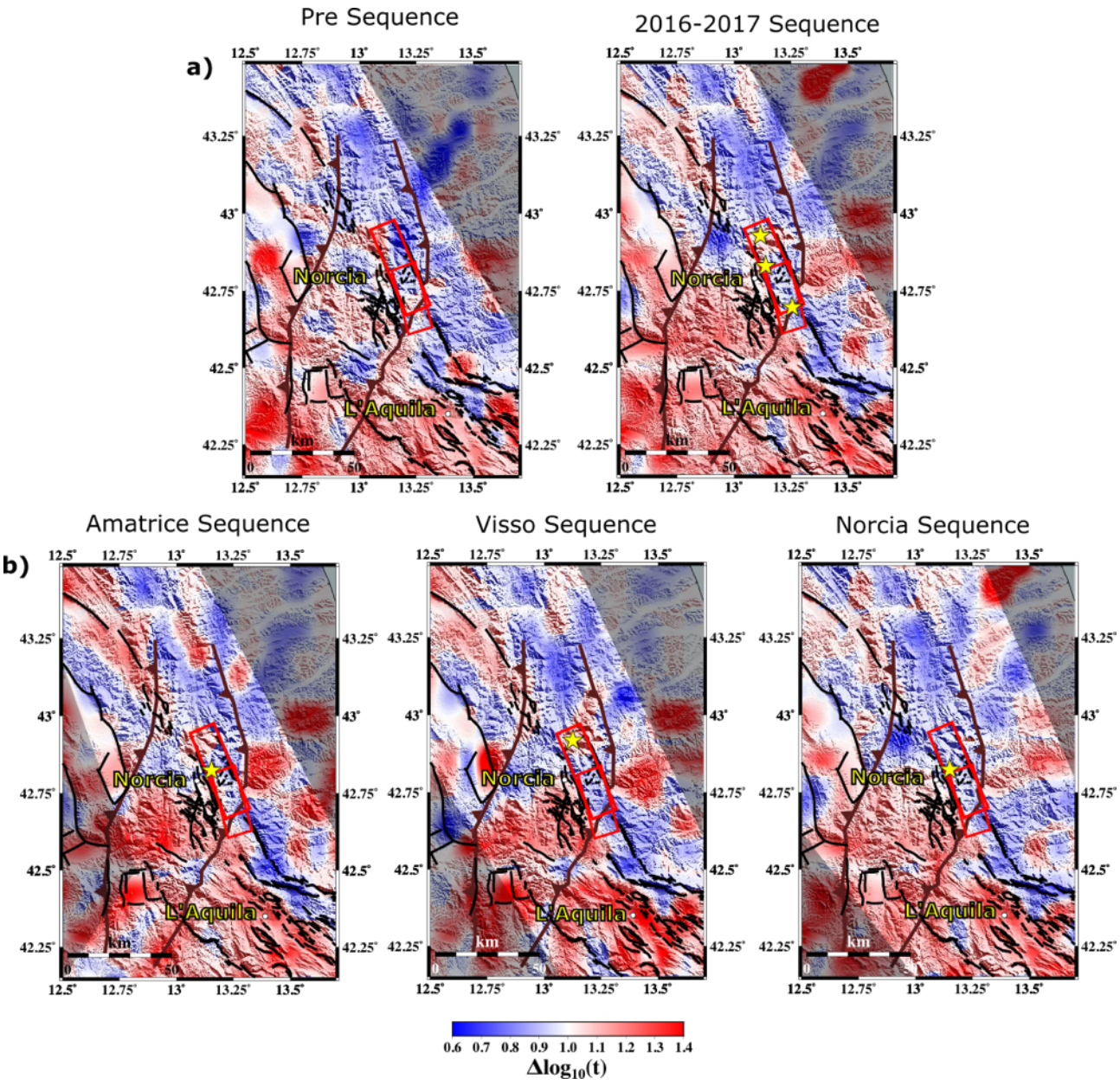

Figure S12 Spatial and temporal variation of Peak Delay at f_c = 12 Hz over the a) Pre-sequence, the 2016-2017 sequence and b) three individual sequences time frames. Red boxes are the fault plane for the Amatrice and the Norcia earthquakes and black lines the faults from ITHACA catalogue. Brown lines are the main thrust of the area. The stars indicate the main shocks of each 2016-2017 sequence. The maps have been restricted to the area of interest.

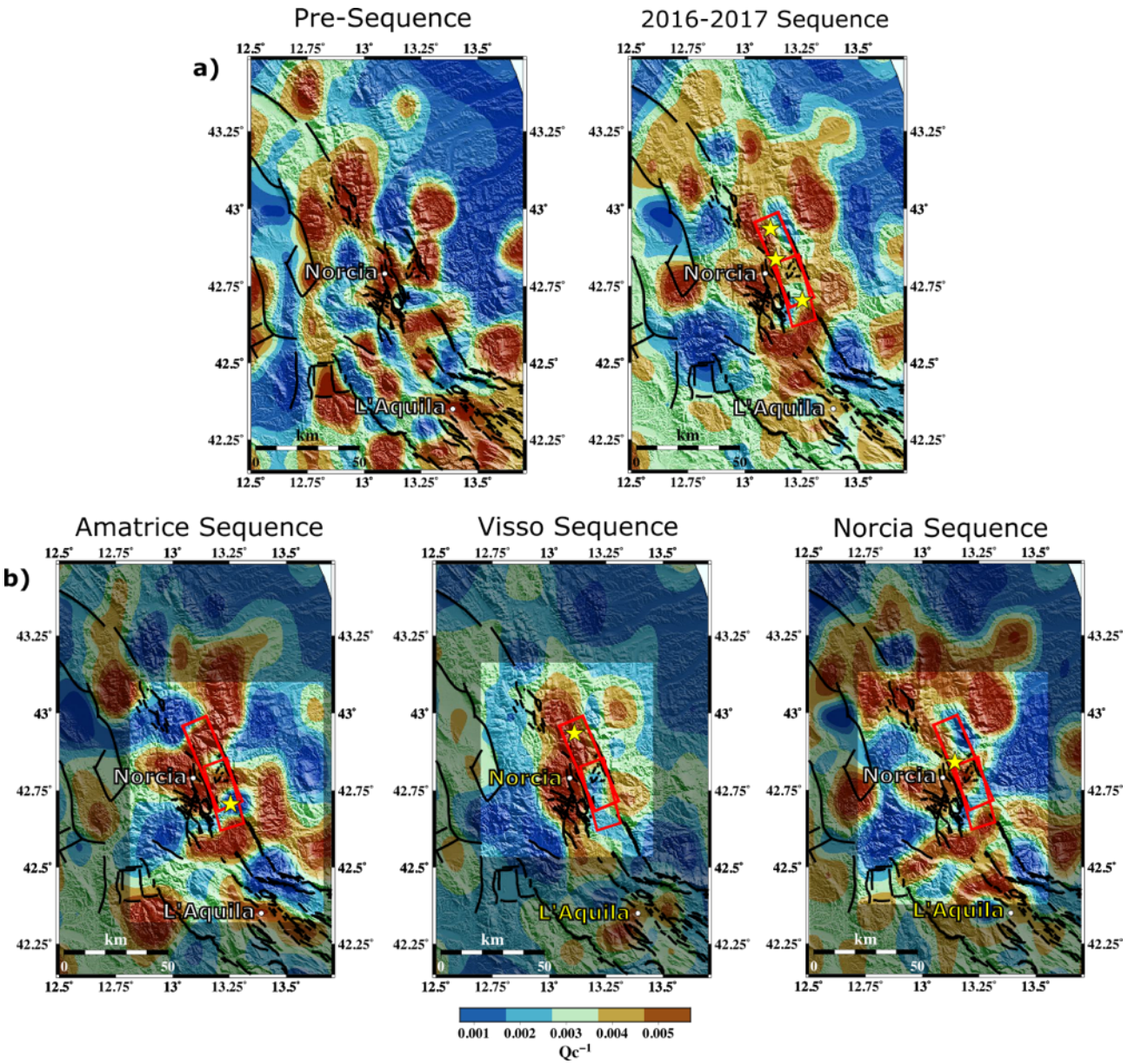

Figure S13 Spatial variation of Q_c^{-1} at f_c = 3 Hz for the a) Pre-sequence and the 2016-2017 sequence and b) three individual sequences time frames. Red boxes are the fault plane activated during the AVN sequence and the black lines are the fault lines from the ITHACA catalogue. The stars indicate the main shocks of each 2016-2017 sequence. The maps have been restricted to the area of interest and the gray masks are covering the areas unresolved by the checkerboard tests at each sequence.

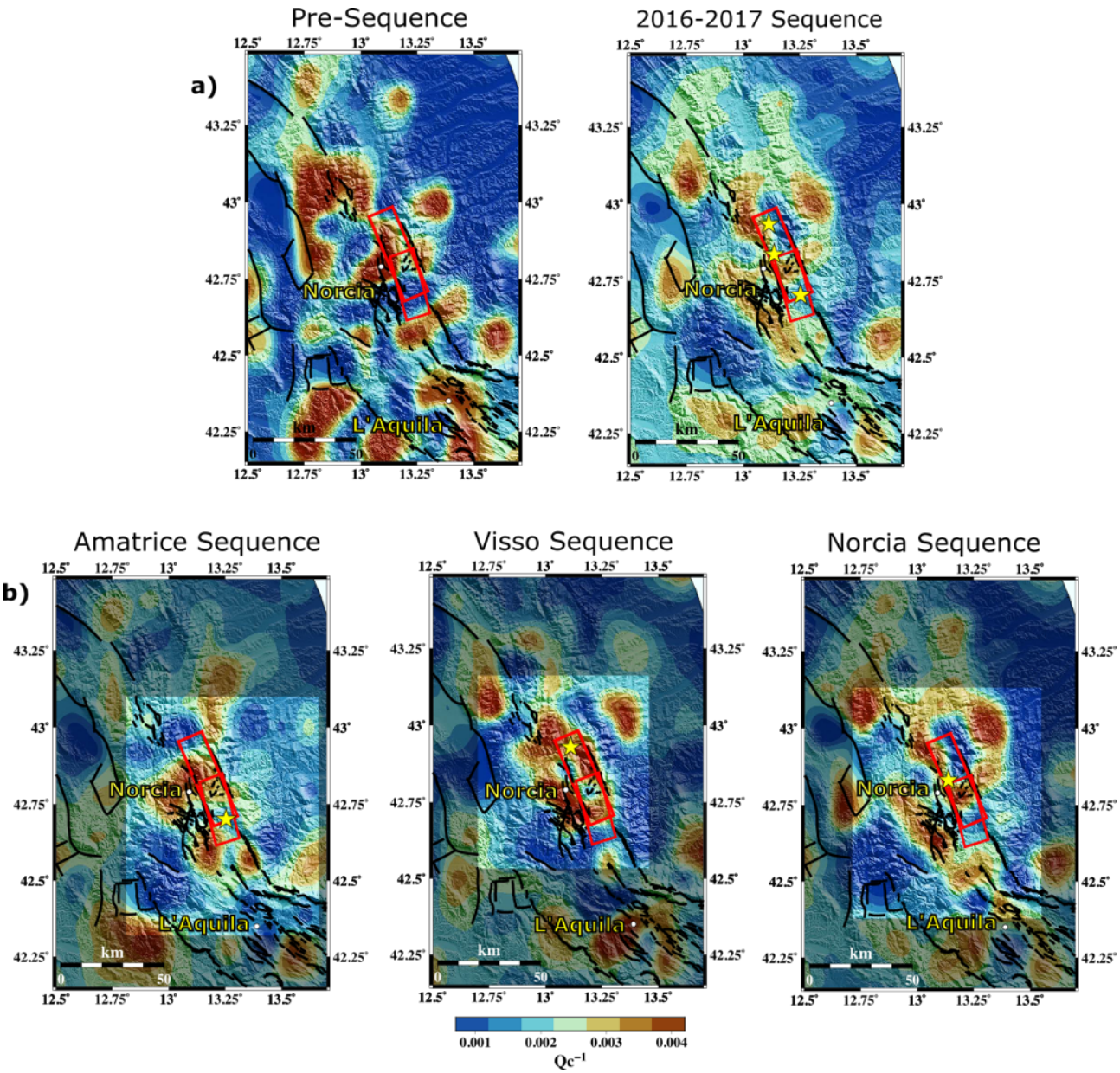

Figure S14 Spatial variation of Q_c^{-1} *at* f_c *= 6 Hz for the a) Pre-sequence and the 2016-2017 sequence and b) three individual sequences time frames. Red boxes are the fault plane activated during the AVN sequence and the black lines are the fault lines from the ITHACA catalogue. The stars indicate the main shocks of each 2016-2017 sequence. The maps have been restricted to the area of interest and the gray masks are covering the areas unresolved by the checkerboard tests at each sequence*

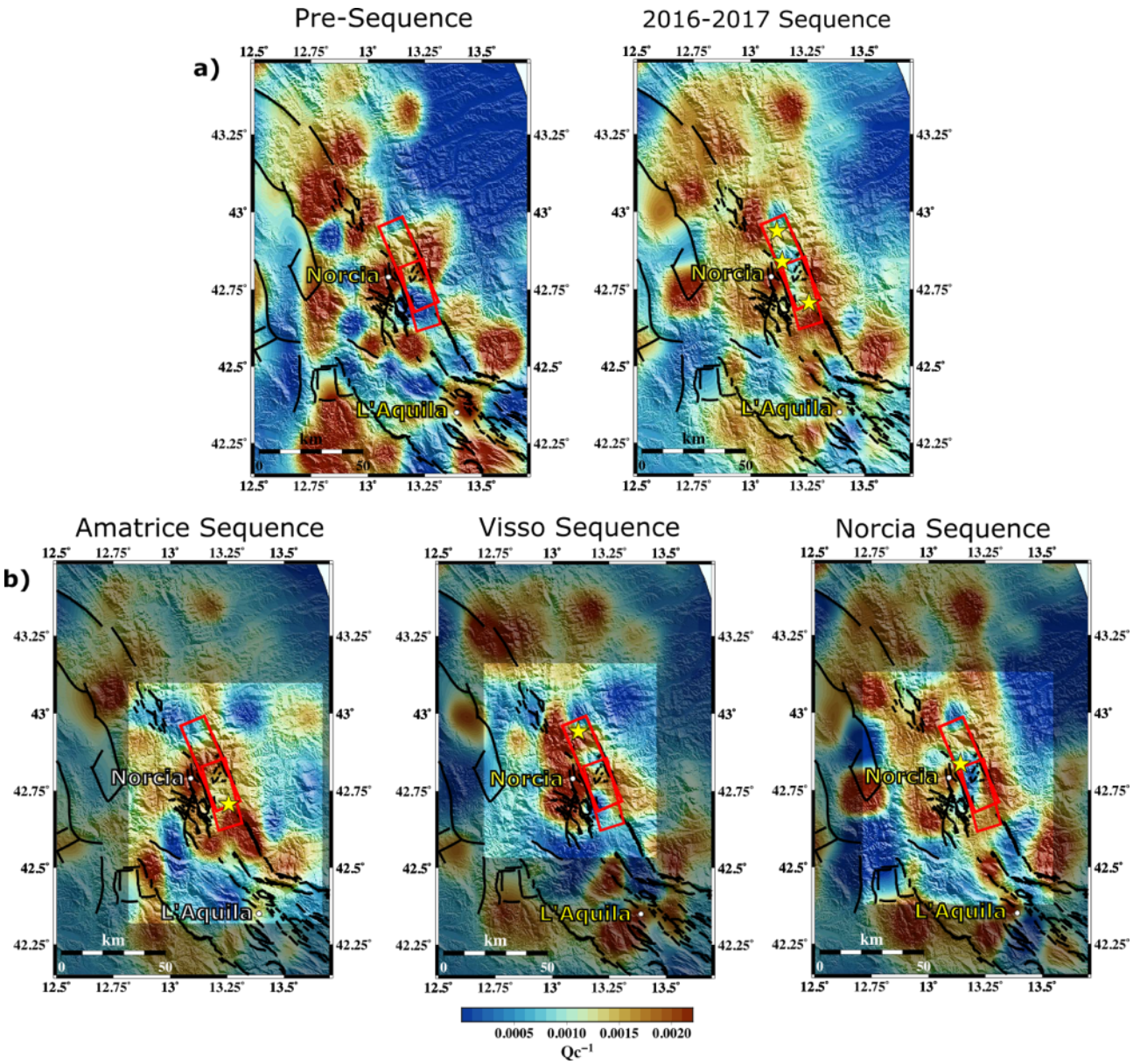

Figure S15 Spatial variation of Q_c^{-1} at f_c = 12 Hz for the a) Pre-sequence and the 2016-2017 sequence and b) three individual sequences time frames. Red boxes are the fault plane activated during the AVN sequence and the black lines are the fault lines from the ITHACA catalogue. The stars indicate the main shocks of each 2016-2017 sequence. The maps have been restricted to the area of interest and the gray masks are covering the areas unresolved by the checkerboard tests at each sequence

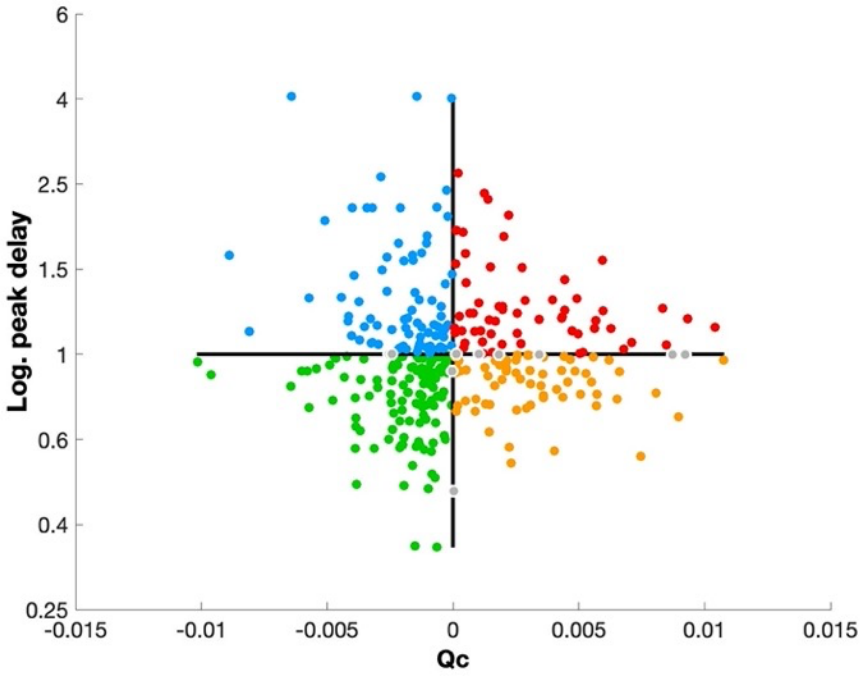

Figure S16 Parameter space separation of the combined absorption (Q_c^{-1}) and scattering (peak delay) attenuation patterns, at fc = 1.5 Hz. The chosen color palette is: red (HS-HA) high scattering and high absorption define a fractured medium saturated in fluids; orange (LS-HA) low scattering and high absorption describe a compact medium filled in fluids; light blue (HS-LA) high scattering and low absorption characterize a dry and fractured medium; green (LS-LA) low scattering and low absorption represent a dry and compact zone medium; grey dots values with a level of discrimination less than 1% of the maximum variations.